Inorganic Chemistry

Article

pubs.acs.org/IC

# Structural Modulations in the Rare-Earth Metal Digermanides $REAl_{1-x}Ge_2$ (RE = Gd−Tm, Lu, Y; 0.8 < x < 0.9). Correlations between Long- and Short-Range Vacancy Ordering

Jiliang Zhang,[†] Yingmin Wang,[‡] and Svilen Bobev*[,†]

[†]Department of Chemistry and Biochemistry, University of Delaware, Newark, Delaware 19716, United States

[‡]School of Materials Science and Engineering, Dalian University of Technology, Dalian 116024, P. R. China

Supporting Information

**ABSTRACT:** Rare-earth metal aluminum germanides with the general formula $REAl_{1-x}Ge_2$ (RE = Gd, Tb, Dy, Ho, Er, Tm, Lu, and Y) have been synthesized by direct fusion of the corresponding elements. The structures have been studied by single-crystal X-ray diffraction and selected-area electron diffraction (SAED). The average structure represents a randomly "stuffed" variant of the orthorhombic $ZrSi_2$ structure type, also known as the $CeNi_{1-x}Si_2$ type (Pearson symbol *o*C16; space group *Cmcm*). The SAED patterns for selected members of the family suggest the coexistence of commensurate and incommensurate structural modulations. The most prominent model for long-range vacancy ordering is the $Tb_4FeGe_8$ type (Pearson symbol *m*P26; space group $P2_1/n$), which is the commensurate 4-fold superstructure of $CeNi_{1-x}Si_2$ ($x = {}^3/_4$). Short-range correlations cause additional deviations in the 4-fold superlattice. These results shed more light on the structural complexity as a function of the aluminum vacancies and size of the rare-earth metal. Magnetic susceptibility measurements are presented and discussed. The measured ordering temperatures and calculated ones based on empirical rules and Ruderman−Kittel−Kasuya−Yosida interactions are shown to be in close agreement.

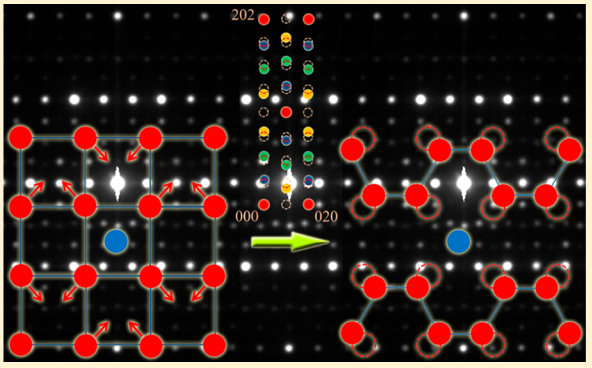


## INTRODUCTION

Fully stoichiometric rare-earth metal digermanides are rare. Among the more than 300 entries in the Pearson Handbook[1] and the *Inorganic Crystal Structure Database (ICSD)*,[2] as of today, there are only four unequivocally established cases of line compounds with the general formula $REGe_2$: $EuGe_2$ ($PtTe_2$ type, space group $P\bar{3}m1$);[3a] $TbGe_2$ (own type, space group *Cmmm*);[3b] $TmGe_2$ and $LuGe_2$ ($ZrSi_2$ type, space group *Cmcm*).[3c] All other reports on the $REGe_2$ phases with either the $\alpha$-$ThSi_2$ (space group $I4_1/amd$)[1] or $AlB_2$ (space group *P*6/*mmm*)[1] structure types, particularly the earlier work done by powder X-ray diffraction (XRD) using film methods, are most likely erroneous. This notion is backed up by the fact that one can easily find significant differences between the properties of samples with structures and compositions presumed to be a match to one another.[4] Structural nuances such as small off-stoichiometry are hard to distinguish based on routine XRD work, and some of the misinterpreted data have propagated in the literature; the cases of mistaken identity can even be seen in the current binary phase diagrams.[5]

Subsequent advances in X-ray crystallography have allowed for the firm realization that the above-mentioned compounds are always substoichiomeric with the general formula $REGe_{2-x}$ ($0.5 < x < 0$).[6] More recently, multiple reports on the partial or full ordering of the vacancies (as opposed to statistical disorder), giving rise to a multitude of superstructures of $REGe_{2-x}$, have appeared.[7] Papers from our laboratories have, for example, described the $RE_3Ge_5$ (i.e., $REGe_{2-x}$ with $x = {}^1/_3$)[7a] and $RE_4Ge_7$ (i.e., $REGe_{2-x}$ with $x = {}^1/_4$)[7b] compounds with structures that exhibit long-range vacancy ordering. The germanides with the formula $RE_3Ge_5$ adopt at least three different structures related to both the $\alpha$-$ThSi_2$ and $AlB_2$ structure types;[1] the $RE_4Ge_7$ germanides are variants of $\alpha$-$ThSi_2$, where commensurate 4-fold superstructures of the $\alpha$-$ThSi_2$ type are seen for RE = Pr, Nd, and Sm,[7b,d,e] while for RE = La and Ce, the structures could not be satisfactorily established from single-crystal X-ray work alone because of coexisting commensurate and incommensurate modulations.

While conducting our research on $REGe_{2-x}$, we noticed that the introduction of a third element to the binary RE−Ge mixtures often yields unexpected outcomes. For example, employing Sn afforded the RESnGe family ($ZrSi_2$ structure type),[8] while the neighboring element In favored a different structural arrangement, as seen for the $RE_2InGe_2$ series ($Mo_2FeB_2$ structure type).[9] Drawing on a prior synthetic experience with $RE[Al_xSi_{1-x}]_2$[10] and $RE[Ga_xSi_{1-x}]_2$,[11] we

Special Issue: To Honor the Memory of Prof. John D. Corbett

Received: April 29, 2014
Published: June 25, 2014

   dx.doi.org/10.1021/ic501002j | Inorg. Chem. 2015, 54, 722−732

Table 1. Selected Crystallographic Data for $REAl_{1-x}Ge_2$ (RE = Gd−Tm, Lu, Y; $0.8 < x < 0.9$)

| empirical formula | $GdAl_{0.22(2)}Ge_2$ | $TbAl_{0.21(2)}Ge_2$ | $DyAl_{0.17(2)}Ge_2$ | $HoAl_{0.16(2)}Ge_2$ | $ErAl_{0.15(2)}Ge_2$ | $TmAl_{0.13(2)}Ge_2$ | $LuAl_{0.10(2)}Ge_2$ | $YAl_{0.17(2)}Ge_2$ |
|---|---|---|---|---|---|---|---|---|
| fw | 308.84 | 309.77 | 312.27 | 314.43 | 316.76 | 317.62 | 322.85 | 239.08 |
| temperature (K) | 200(2) | | | | | | | |
| radiation | Mo K$\alpha$, $\lambda$ = 0.71073 Å | | | | | | | |
| space group | *Cmcm* (No. 63), $Z = 4$ | | | | | | | |
| $a$ (Å) | 4.1471(16) | 4.1499(11) | 4.0823(8) | 4.073(3) | 4.0656(15) | 4.0353(10) | 4.0097(7) | 4.1059(10) |
| $b$ (Å) | 16.460(6) | 16.334(16) | 16.218(3) | 16.097(10) | 16.018(6) | 15.875(4) | 15.708(3) | 16.301(4) |
| $c$ (Å) | 3.9711(15) | 3.9712(10) | 3.9330(7) | 3.927(3) | 3.9199(14) | 3.8983(9) | 3.8766(7) | 3.9465(10) |
| $V$ (Å$^3$) | 271.08(18) | 269.19(12) | 260.39(8) | 257.4(3) | 255.28(16) | 249.73(10) | 244.16(8) | 264.15(11) |
| $\rho_{cal}$ (g cm$^{-3}$) | 7.56 | 7.64 | 7.97 | 8.11 | 8.24 | 8.44 | 8.78 | 6.01 |
| $\mu$ (cm$^{-1}$) | 459.1 | 478.6 | 510.0 | 533.0 | 556.2 | 587.8 | 641.9 | 440.7 |
| R1 [$I > 2\sigma(I)$][a] | 0.0246 | 0.0231 | 0.0206 | 0.0207 | 0.0170 | 0.0202 | 0.0159 | 0.0248 |
| wR2 [$I > 2\sigma(I)$][a] | 0.0516 | 0.0547 | 0.0527 | 0.0467 | 0.0371 | 0.0449 | 0.0394 | 0.0585 |

[a] $R1 = \sum||F_o| - |F_c||/\sum|F_o|$, $wR2 = \{\sum[w(F_o^2 - F_c^2)^2]/\sum[w(F_o^2)^2]\}^{1/2}$, where $w = 1/[\sigma^2F_o^2 + (AP)^2 + BP]$, with $P = (F_o^2 + 2F_c^2)/3$; $A$ and $B$ are weight coefficients.

expected similar trends with regard to $RE[Al_xGe_{1-x}]_2$; however, the earlier experiments with these elements led to the identification of $RE_2AlGe_2$ with the $W_2CoB_2$ structure type.[12] At that time, the $REAl_{1-x}Ge_2$ phases were obtained as minor products.[12]

With this paper, we report the results from our detailed investigations on the latter series of compounds (RE = Y, Gd−Tm, Lu). $REAl_{1-x}Ge_2$ are isotypic with many digermanides containing transition metals,[13,14] with a structure type known as $CeNi_{1-x}Si_2$.[1] The existence of some of these phases had been noted in publications from 2008, but the very short (unphysical!) distance between Ge (full occupancy) and the partially occupied Al had not received proper attention. Similar problems are also known in the $RET_{1-x}Ge_2$ (T = transition metal) structures, and several detailed crystallographic studies have uncovered weak modulations, such as the proposed 4-fold superstructure model $Tb_4FeGe_8$.[15] Compared with the transition metals reported to form compounds with this structure, Al has much lower melting temperature, making the $REAl_{1-x}Ge_2$ compounds ideal to study the issues pertaining to the structure and its apparent dependence of the homogeneity range with the nature of the rare-earth metal. The fact that Al has no d electrons can contribute to the unraveling of the rich magnetism displayed by the compounds forming with this "average" structure.

## EXPERIMENTAL SECTION

**Synthesis.** All manipulations were performed inside an Ar-filled glovebox with oxygen and moisture levels of less than 1 ppm or under vacuum. The starting materials, rare-earth metals (pieces, 99.9 wt % metal basis, Alfa-Aesar), Ge (lump, 99.999 wt %, Acros), and Al (shot, 99.999 wt %, Alfa-Aesar), were used as received. The reactions were carried out using an arc melter under a Ti-gettered Ar atmosphere. All samples were prepared from elemental mixtures with nominal stoichiometry $RE_2AlGe_4$. Each "button" was remelted at least three times to ensure the compositional homogeneity and the weight loss from the processing was always less than 1 wt %. Following arc melting, the obtained materials were sealed within fused silica ampules under vacuum. All samples were quickly (rate 200 K h$^{-1}$) heated to 750 °C and annealed at this temperature for 2 weeks. At the end, the ampules were taken out of the furnace and allowed to cool to room temperature.

The outcomes of these experiments were monitored by powder and single-crystal XRD; the products were nearly single phase (>90% estimated) with refined formulas $REAl_{1-x}Ge_2$ (RE = Gd−Tm, Lu, Y; $0.8 < x < 0.9$) slightly different from the loading compositions $REAl_{0.5}Ge_2$. In addition, mixtures of the constituent elements, adjusted to the refined compositions and processed following the above routes, yielded no statistically significant differences in the refined unit cell volumes and/or compositions.

**Powder XRD.** Powder XRD patterns were taken at room temperature on a Rigaku MiniFlex powder diffractometer using filtered Cu K$\alpha$ radiation. The obtained patterns were then compared with the calculated patterns based on the corresponding single-crystal structures, and they matched each other very well (see Figure S1 in the Supporting Information, SI).

**Single-Crystal XRD.** Breaking the annealed ingots revealed small, silvery crystals, which were cut under a microscope to ca. 0.03−0.07 mm in all dimensions. They were picked out and placed on glass fibers using Paratone N oil. Intensity data sets were collected at 200 K on a Bruker SMART CCD diffractometer equipped with monochromated Mo K$\alpha$ radiation. The data collection routine in *SMART*[16] with scans at different $\omega$ and $\phi$ angles allowed for full coverage of the reciprocal space up to $\sin\theta/\lambda \approx 0.75$ Å$^{-1}$. The collected frames were integrated using the *SAINTplus* program.[17] *SADABS* was used for semiempirical absorption correction based on equivalents.[18] The structure refinements were carried out by full-matrix least-squares methods on $F^2$, as implemented in *SHELXTL*.[19]

Several observations with regards to the single-crystal XRD studies deserve a special mention. First, indexing the diffraction data was straightforward; the structures could be readily solved by direct methods in the space group of choice, *Cmcm* (Table 1). Initially, the atomic positions of the rare-earth atoms and the Ge atom were located by direct methods, revealing the $ZrSi_2$-type structure (Pearson code *oC*12).[1] Subsequent refinements showed a peak of moderate height (8−10 e Å$^{-3}$) located ca. 2.1−2.2 Å away from one of the Ge atoms, Ge2. When this site (partially occupied) is included in the model, the structure becomes identical with those adopted by many $RET_{1-x}Ge_2$ (T = transition metal) compounds,[13,14] also known as the $CeNi_{1-x}Si_2$ structure type (Pearson code *oC*16).[1]

This model poses several challenges. First, because of the low electron density and relatively short distances to neighboring atoms, a light nonmetallic element such as O may seem a possible fit; it could be ruled out based on its 5-fold coordination to Ge atoms. The height of the peak was varied with the nature of the rare-earth metal (higher for the one near the middle of the 4f series and lower for the very heavy ones). Second, Ge could also be assigned at that partially occupied position, in accordance with the reported structure of $ErGe_{2.16}$;[20] however, because elemental analyses by energy-dispersive X-ray (EDX) spectrometry confirm the presence of Al, assignment of the position as partially occupied Al is more reasonable. The latter argument can be countered by the resultant short Ge2−Al distance and the oblate thermal displacement parameters of the Ge atoms; these traits have been noted in the past from refinements of the $RET_{1-x}Ge_2$ structures.[13,14] Notice that the Ge2 site has an occupation factor that does not deviate from unity when freed, which means that evoking occupational disorder cannot provide a plausible explanation.


dx.doi.org/10.1021/ic501002j | Inorg. Chem. 2015, 54, 722−732

Long-exposure zone images (300−900 s), taken on the CCD diffractometer, did not show any "streaking" or other problems, and credible superstructure reflections were not apparent. Attempts to integrate the reflections from the single-crystal data into the 4-fold monoclinic superstructure proposed for $Tb_4FeGe_8$[15] were not successful. This work led to unsatisfactory residuals, suggesting that the vacant Al sites in the crystal structure are not long-range-ordered as in $Tb_4FeGe_8$.[15] Therefore, we sought the help of electron diffraction to gain further insight into the structure. The search for possible (in)commensurate modulation is addressed later in the transmission electron microscopy (TEM) part of this paper, while the X-ray data were worked out as the "average" $REAl_{1-x}Ge_2$ (RE = Gd−Tm, Lu, and Y; $0.8 < x < 0.9$) structures with the $CeNi_{1-x}Si_2$ structure type.[1] A list of important crystallographic parameters and details for these refinements are summarized in Table 1. Final positional and isotropic thermal parameters and important distances of $TbAl_{0.21(2)}Ge_2$ (chosen as a representative for discussion and direct comparison with $Tb_4FeGe_8$[15]) are listed in Tables 2 and 3, respectively. A combined crystallographic information file (CIF) of all compounds is provided as SI.[21]

**Table 2. Atomic Coordinates and Equivalent Isotropic Displacement Parameters ($U_{eq}$[a]) of $TbAl_{0.21(2)}Ge_2$**

| atom | site | $x$ | $y$ | $z$ | $U_{eq}$ (Å$^2$) |
|---|---|---|---|---|---|
| Tb | 4c | 0 | 0.39610(5) | $^1/_4$ | 0.007(1) |
| Ge1 | 4c | 0 | 0.0495(1) | $^1/_4$ | 0.013(1) |
| Ge2 | 4c | 0 | 0.7516(1) | $^1/_4$ | 0.035(1) |
| Al[b] | 4c | 0 | 0.190(1) | $^1/_4$ | 0.009(7) |

[a] $U_{eq}$ is defined as one-third of the trace of the orthogonalized $U^{ij}$ tensor. [b] Refined occupancy is 0.21(2).

**Table 3. Selected Interatomic Distances in $TbAl_{0.21(2)}Ge_2$**

| atom pair | distance (Å) | atom pair | distance (Å) |
|---|---|---|---|
| Ge1−Ge1 (×2) | 2.560(3) | Tb−Ge1 (×4) | 3.0065(8) |
| Ge2−Ge2 (×4) | 2.872(2) | Tb−Ge2 (×2) | 3.125(2) |
| Ge1−Al | 2.29(2) | Tb−Al (×4) | 3.197(9) |
| Ge2−Al (×2) | 2.204(9) | | |

**Electron Microscopy.** Microscopy studies aimed to verify the compositions by EDX spectrometry were carried out using a JEOL 7400 F electron microscope equipped with an INCA-Oxford spectrometer. The microscope was operated at 10 $\mu$A beam current at 15 kV accelerating potential. Data were acquired on small crystallites, mounted onto carbon tape. Several areas on the same crystal were probed and averaged. The obtained results (provided as SI) are in good agreement with the refined compositions. Additionally, elemental mapping confirms the homogeneity of the samples.

To inspect the possible superlattices in the compound, selected-area electron diffraction (SAED) data were gathered using a Philips TECNAI 20 G2 transmission electron microscope operated at 200 kV and using acquisition times between 60 and 90 s. All samples for TEM were prepared by first grinding the crystals, suspending the powder in ethanol, and applying 1−2 drops of solution to a 200- or 300-mesh copper grid, coated with a lacey-carbon film. Such a procedure is not expected to introduce structural faults (or variations) because of the brittleness of the samples.

**Thermal Analysis.** Thermal analysis was conducted using a SDT Q600 instrument. To prevent oxidation, analysis was performed in a flow of high-purity argon. Approximately 30 mg of a polycrystalline $TbAl_{0.21(2)}Ge_2$ sample was used for the experiment. Heating and cooling rates were set at 15 °C/min. As shown in Figure S2 in the SI, the onset of an endothermal event upon heating is at 843 °C (melting), which is much lower than the melting temperatures of binary $TbGe_2$ or $TbGe_{2-x}$ but higher than that of $TbGe_{3-x}$, according to the phase diagrams.[5] The formation of another, yet unknown phase upon cooling is evident and also confirmed by the powder XRD in Figure S1 in the SI.

**Magnetic Susceptibility.** Field-cooled and zero-field-cooled direct-current magnetization ($M$) measurements were completed using a Quantum Design MPMS SQUID magnetometer in the temperature range 5−350 K and in an applied field ($H$) of 500 Oe. For all of these measurements, the samples were secured in a custom-designed low-background sample holder. The raw magnetization data were corrected for the holder contribution and converted to molar susceptibility ($\chi_m = M/H$).

**Electronic Structure Calculations.** Tight-binding linear muffin-tin orbital calculations were performed in the atomic sphere approximation.[22] Two cases were considered: the idealized $YGe_2$ and $Y_4AlGe_8$ compounds with ordered and optimized structures. The radii of the Wigner−Seitz spheres were assigned automatically so that the overlapping potential would be the best possible approximation to the full potential.[23] They were determined as follows: Y, 1.903−1.960 Å; Al, 1.406 Å; Ge, 1.431−1.486 Å. $k$-space integrations were conducted by the tetrahedron method,[24] and the self-consistent charge density was obtained using 12 × 12 × 12 and 4 × 2 × 2 $k$ points in the Brillouin zones for $YGe_2$ and $Y_4AlGe_8$, respectively. Exchange and correlation were treated by the local density approximation,[25] and all relativistic effects were taken into account using the scalar relativistic approximation,[26] except spin−orbit coupling. To interrogate the chemical bonding, crystal orbital Hamilton populations (COHPs) of selected interactions were also analyzed.[27]

Total energy calculations and structural optimization for $YGe_2$ and $Y_4AlGe_8$ were performed with the first-principles pseudopotential based density functional theory, as implemented in SIESTA,[28,29] which employs a localized orbital basis in the representation of wave functions. The soft norm-conserving pseudopotential and the Perdew−Berke−Emzerhof exchange correlation energy within the generalized gradient approximation were utilized.[30,31] The optimizations are deemed to have sufficiently converged when the residual forces on any atoms are smaller than 0.001 eV Å$^{-1}$.

## RESULTS AND DISCUSSION

**Structure and Bonding.** The "average" structure of the title compounds $REAl_{1-x}Ge_2$ (RE = Gd−Tm, Lu, Y; $0.8 < x < 0.9$), as elucidated by XRD, can be described as a randomly "stuffed" variant of the orthorhombic $ZrSi_2$ structure type, also known as the $CeNi_{1-x}Si_2$ type (Pearson symbol $oC16$; space group $Cmcm$).[1] The digermanides $RET_{1-x}Ge_2$ are well-known and have been realized with most first-row transition metals (T) from Cr to Cu.[13,14] Currently, Al appears to be the only post-transition metal to form compounds with this structure.

There are four independent sites in the asymmetric unit (Table 2): one is for the rare-earth atom and two are for the Ge atoms, which are all fully occupied; these three describe the $ZrSi_2$ structure. The fourth site is occupied by Al atoms only about $^1/_5$ of the time (vide supra); this is the equivalent of the partially occupied Ni position in the archetype $CeNi_{1-x}Si_2$.[1]

We should mention that, prior to our work in these systems, other research groups had initiated structural studies and had already reported on $REAl_{1-x}Ge_2$ (RE = Gd, Ho, and Er; $x$ = 0.65),[32] all done by Rietveld refinements. The three compounds from the latter report are compositionally similar to our $GdAl_{0.22(2)}Ge_2$, $HoAl_{0.16(2)}Ge_2$, and $ErAl_{0.16(2)}Ge_2$ (Table 1). In 2006, however, another group had reportedly identified the phases $REAl_{0.15}Ge_{1.85}$ (RE = Tb, Dy, and Ho) also by powder XRD.[33] They have been suggested to be variants of the $ZrSi_2$ structure type with positional Ge/Al disorder.[33] Our results suggest the possible erroneous interpretation of the earlier data; it could be argued that the latter phases are identical with the ones discussed herein and that the small


dx.doi.org/10.1021/ic501002j | Inorg. Chem. 2015, 54, 722−732

differences in the unit cell volumes are likely due to the differences in the data collection temperatures, not structural variations. Here, we correct the discrepancies and also extend the $REAl_{1-x}Ge_2$ series to include the Tb, Tm, Lu, and Y analogues.

The structure is schematically presented in Figure 1. The structure can be described starting with a "parent" $REGe_2$

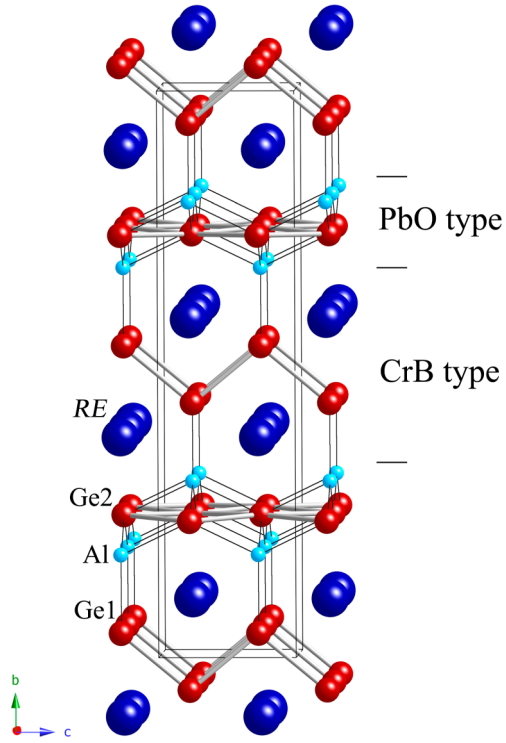


**Figure 1.** Idealized crystal structure of $REAlGe_2$ (disorder-free), viewed down the *a* axis. The structure is orthorhombic, with space group *Cmcm*, and can be viewed as an intergrowth of PbO- and CrB-type slabs. The rare-earth metal atoms are shown as dark-blue spheres, the Ge atoms are drawn as maroon spheres, and the Al atoms are shown in light blue, respectively. The unit cell is outlined.

structure ($ZrSi_2$ structure type, known as such only for $TmGe_2$ and $LuGe_2$),[3c] and simply inserting Al into it. In the idealized crystal structure of $REAlGe_2$, there are no vacant Al sites and the Al atoms cap the Ge square nets (site Ge2) above and below in an alternating fashion, producing a slab with the topology of the PbO-type layers.[1] This slab is sandwiched between slabs, which have Ge zigzag chains (site Ge1), running parallel to the crystallographic *c* axis; each Ge atom from the chains is located at the center of a trigonal prism of rare-earth metal atoms (Figure 1). This arrangement is reminiscent of the monogermanides REGe, forming with the CrB structure type.[34]

However, the above description is deceptively simple. First, there are more vacant Al positions than occupied (the site occupation factor is on the order of 16−22%). Second, the resultant Al−Ge distances are anomalously short. Taking $TbAl_{0.21(2)}Ge_2$ as an example (Table 3), one can see that the shortest Al−Ge distance is only 2.204(9) Å, much shorter than the sum of the Pauling radii of the two elements ($r_{Al}$ = 1.248 Å; $r_{Ge}$ = 1.242 Å).[35] This, coupled with the pronounced enlargement of the Ge2 anisotropic displacement parameter in the *ac* plane ($U_{11} \approx U_{33} > U_{22}$), is suggestive of unresolved structural disorder. On the other hand, the Ge−Ge and RE−Ge distances do not show anything out of the ordinary, and their values are typical for those found in related germanide structures.[3,7−15] As expected, the Ge1−Ge1 distance within the zigzag chains is 2.560(3) Å, shorter than the Ge2−Ge2 distance within the square nets, which measures 2.872(2) Å. The reason these contacts are longer than the typical values for Ge−Ge single bonds is that each Ge is nearly square-planar, and the bonding ought to be treated as hypervalent, as discussed in detail elsewhere.[36,37] It appears though that such hypervalent interactions can be intimately affected by neighboring elements, which is the case with the $RET_{1-x}Ge_2$ phases (T = Cr−Cu); the Ge−Ge distances within the square nets are even longer in such structures with transition metals,[13,14] compared to their $REAl_{1-x}Ge_2$ counterparts. The effect has complex origins because it appears that the Ge−Ge distances vary as a function of the nature of the element, the nature (size) of the rare-earth metal, or both. In cases where phases with varied stoichiometry breadth exist, a dependence on "*x*" can be also seen. The above may suggest that a multicenter bonding, as discussed for $BaAl_4$-type and related structures,[36] might play a role here and deserves a more careful consideration.

The enlargement of the anisotropic displacement of Ge2, mentioned in the previous paragraph, may actually be an indication of a distortion in the square net: the Ge2−Ge2 distance can and must vary locally because the Ge square net is not "big enough" to accommodate the capping Al atoms. We argue that, as the unit cell volume decreases as a function of the lanthanide contraction, this effect becomes even more pronounced and the shortest Al−Ge distances become ca. 2.15 Å, in correlation with the decrease in the occupancy of Al; it is about $^1/_5$ in $TbAl_{0.21(2)}Ge_2$ and drops to only about $^1/_{10}$ in $LuAl_{0.10(2)}Ge_2$. Distortion of the squares and creating pattern of shorter (bonding) and longer (nonbonding) interactions could alleviate this problem, and one plausible way of doing it is illustrated in Figure 2. As a result, the square net of Ge atoms is

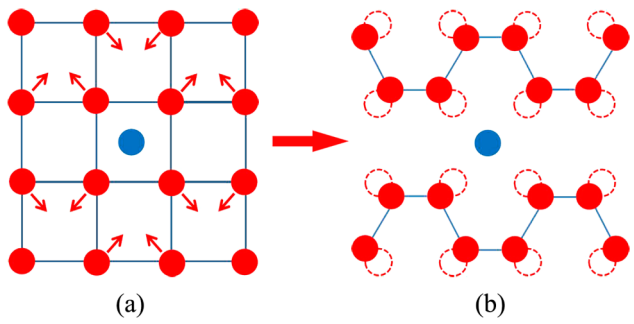


**Figure 2.** Schematic illustration on the structural variation from Ge square nets (a) to parallel cis−trans chains (b) induced by the inset Al atom. The red circles represent the Ge atoms, and the blue circle shows the projection of an Al atom onto the plane. Arrows in part a indicate shifts of the Ge atoms from their averaged position. The dotted circles in part b mark the ideal positions for the square nets.

broken into arrays of parallel cis−trans chains. This array is similar to that in $Tb_4FeGe_8$ with a 4-fold monoclinic superstructure.[15] We should also point out the fact that square nets are prone to a Pierels distortion, as computationally shown by Hoffmann et al., and a transformation to parallel cis−trans chains has been reported as one of the most likely outcomes.[37] However, it is only one of the simplest possible configurations, and the details should depend on the third element, as well as


dx.doi.org/10.1021/ic501002j | *Inorg. Chem.* 2015, 54, 722−732

the "$x$" value in $REAl_{1-x}Ge_2$. A similar dependence on the occupation factor of Li in $RELi_{1-x}Sn_2$ (the same structure type as $REAl_{1-x}Ge_2$ but realized with the light rare-earth metals) was also reported recently.[38] Notice that the disorder described for $RELi_{1-x}Sn_2$ is in the chains, not in the square nets, which could be due to the fact that s−p mixing in Sn is poorer and Sn favors hypervalent bonding.

The anisotropic displacement parameters for the Ge1 atoms are also elongated, but to a smaller degree and in a different direction; the Ge1 site shows a larger displacement along the $b$ axis, with the mean-square displacement twice that in the other directions (Table S3 in the SI). Using the same arguments as those stated above, we can propose again some averaging of positions within the zigzag chains to ease the strain from the short Al−Ge contacts. This point is easier to demonstrate with the monoclinic $Tb_4FeGe_8$ superstructure, where the Ge atoms forming the chains are on four independent sites. Structure optimization for hypothetical $Y_4AlGe_8$, as presented in the Tables S4 and S5 in SI, shows very reasonable thermal displacement and Al−Ge1 distances.

**Electron Diffraction.** The "average" structure from refinement of the XRD data poses problems and clearly suggests possible modulations. To uncover long-range defect ordering, TEM and SAED were employed, and the work was mainly done on $TbAl_{0.21(2)}Ge_2$. Several crystals from the same reaction batch were examined, and their SAED patterns show satellite reflections. Figure 3 presents the stereoarrangement of SAED

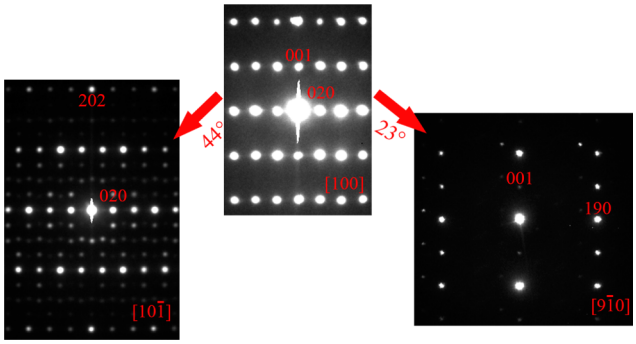


**Figure 3.** Stereoarrangement of the SAED patterns in $TbAl_{0.21(2)}Ge_2$. The left shows the rotation along the $b$ axis, and the right presents the rotation along the $c$ axis. The satellite reflections are evident in both low- and high-index zones.

patterns obtained on an individual crystal; the indexing routine using the strong reflections only yields an orthorhombic symmetry with the lattice parameters $a$ = 4.2 Å, $b$ = 16.6 Å, and $c$ = 4.0 Å, in good agreement with the XRD data in Table 1. The [100] zone shows no discernible satellite reflections, and the angle between the $b$ and $c$ axes is 90.0(2)°, also corroborating the orthorhombic symmetry. The SAED pattern does not appear to indicate any evidence for a monoclinically distorted structure, as previously reported for $Tb_4FeGe_8$.[15] However, the rotations along the $a$ and $b$ axes both show evidence for satellite reflections, as seen in the [10$\bar{1}$] and [9$\bar{1}$0] zones, respectively.

In the [10$\bar{1}$] zone, satellite reflections are shown clearly, as emphasized in the SAED patterns of Figure 4. The superstructure is roughly characterized by a vector $q$ = 1/8(202) = ($^1/_4$, 0, $^1/_4$). Such quadrupling of the unit cell is in good agreement with the monoclinic model, previously discussed for $Tb_4FeGe_8$.[15] However, closer examination on the SAED

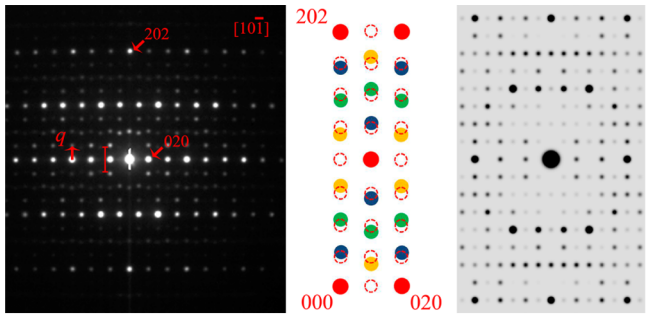


**Figure 4.** SAED pattern along the [10$\bar{1}$] zone axis (left) showing satellite reflections for $TbAl_{0.21(2)}Ge_2$, compared to the simulated [100] zone axis pattern for the hypothetical monoclinic $Tb_4AlGe_8$ (right panel). In the experimental SAED pattern, the wave vector for the modulation $q$ is marked with a small vertical arrow. The schematic illustration in the middle depicts the incommensurate order for the superstructure. Here, the blue, green, and yellow dots represent the first-, second-, and third-order satellite reflections, respectively. The circles drawn with dashed lines stand for theoretically predicted satellites for a commensurate long-range order.

pattern shows that the modulation is actually incommensurate. The hallmark of such an incommensurate modulation is the row of reflections nearly halfway between the reflections corresponding to the 4-fold superstructure. For example, in Figure 4, the existence of two weak satellites to the mean peaks in the SAED pattern is marked with the red vertical line shown; notice the different modulation lengths on both sides of the red bar. Such fluctuations also exist in other rows of satellites but are hard to discern on the viewgraph because of the very low intensity of the satellites. For a better illustration, in the middle panel of Figure 4, we have also plotted the commensurate modulations corresponding to the [100] zone in the monoclinic $Tb_4FeGe_8$ structure, that is, the circles shown with dashed lines. The experimentally observed reflections are drawn as filled circles, and they clearly deviate from the ideal positions.

In the high-index [9$\bar{1}$0] zone, the modulated reflections are also clear, as shown by the SAED pattern in Figure 5. The weak satellites are consistent with a nearly quadrupled indexing, and the modulation wave vector can be expressed as either $q'$ = 1/4(193) or $q''$ = 1/4(191). Again, the modulations are not commensurate, and this point is reaffirmed in the schematic representation of the diffraction pattern; these satellite reflections deviate from the commensurate positions (circles with dashed lines), corresponding to the [6$\bar{1}$3] zone of the $Tb_4FeGe_8$ structure. The simulated SAED patterns for the $CeNi_{1-x}Si_2$ (I, [9$\bar{1}$0] zone) and $Tb_4FeGe_8$ (II, [6$\bar{1}$3] zone, corresponding to the [9$\bar{1}$0] zone in the parent structure) structures are also shown in Figure 5. Apart from the incommensurate modulations, there are two other noteworthy differences: (1) when $l$ is odd, the calculated (19$l$) reflections are very weak, but the observed ones in the SAED patterns are strong; (2) the strongest satellites in the simulation are those that "half" the parent reflections, while the strongest ones in the observation appear at the quarter. Recall that this was also the case in the [10$\bar{1}$] zone, as presented in the previous paragraph and in Figure 4. Accordingly, the observed structure can be considered as an intermediate state between $TbAl_{1-x}Ge_2$ ($CeNi_{1-x}Si_2$ structure) with randomized defects and its 4-fold $TbAl_{0.25}Ge_2$ superstructure ($Tb_4FeGe_8$ structure) with fully ordered defects.


dx.doi.org/10.1021/ic501002j | Inorg. Chem. 2015, 54, 722−732

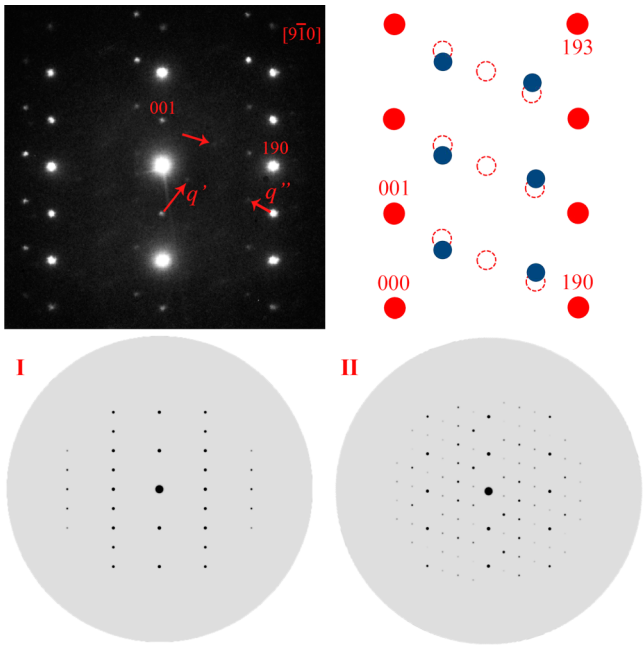


**Figure 5.** SAED pattern corresponding to a high-index [9$\bar{1}$0] zone in $TbAl_{0.21(2)}Ge_2$. In the schematic diagram with the reflections, blue dots represent the first-order satellite reflections and dashed circles denote the calculated positions of the satellite reflections corresponding to the quadruple commensurate modulation. Two arrows marked as $q'$ and $q''$ point to the faint second-order satellite reflections. The simulated patterns are for the [9$\bar{1}$0] zone of the orthorhombic $CeNi_{1-x}Si_2$-type structure (I) and the [6$\bar{1}$3] zone of the monoclinic $Tb_4FeGe_8$ superstructure (II).

Although one may argue that the SAED data from Figures 4 and 5 point to crystal quality issues and coprecipitation of a "kinetic" phase along with the "thermodynamic" product, we note that two additional weeks of annealing did not yield improvements. It can be countered that either (1) further equilibration is required to remedy the "faults" in the crystal-growth process or (2) this is an inherent feature. Our current thinking is that, because very few of the reported $RET_{1-x}Ge_2$ (T = transition metal) show long-range ordering (despite the use of a multitude of synthetic/annealing techniques),[13,14] the latter supposition is more likely. Further experimental evidence that also lends support to this hypothesis is the fact that the "$x$" value in $REAl_{1-x}Ge_2$ varies with the rare-earth metal; i.e., the phases are likely in equilibrium, but other factors influence the long-range and local structures. We did not complete thorough electron diffraction investigations on all $REAl_{1-x}Ge_2$ samples, but most of the collected SAED patterns are in agreement with the notion of incommensurate modulations; nearly commensurate modulations were also observed (several SAED patterns for two independent crystals are shown in Figure S4 in the SI). The existence of both lower-order (Figure S4a in the SI) and higher-order (Figure S4b in the SI) modulations should also be noted.

On this note, it is informative to compare the SAED patterns of $TbAl_{0.21(2)}Ge_2$ and $HoAl_{0.16(2)}Ge_2$. The refined Al content between them is within the limits of $3\sigma$ and could be dismissed as statistically insignificant. However, this could very well be the reason why there are no visible satellites in the [1$\bar{1}$0] zone for the latter (Figure 6). Upon moving to the [5$\bar{1}$0] zone, several weak satellite reflections are seen. It should be noted that the satellite reflection is not in the middle of two adjacent parent reflections but rather close to the weak one.

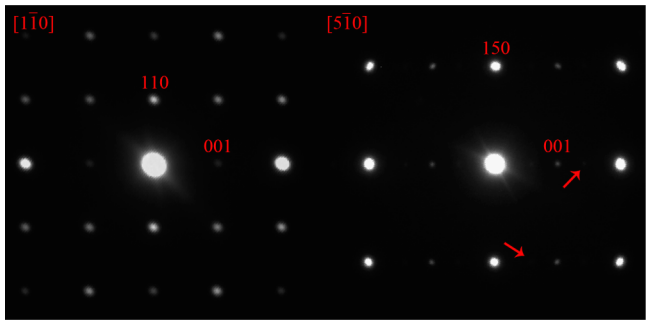


**Figure 6.** SAED patterns corresponding to the [1$\bar{1}$0] and [5$\bar{1}$0] zones in $HoAl_{0.16(2)}Ge_2$. The arrows within the [5$\bar{1}$0] zone indicate the weak superlattice reflections.

As discussed in the previous section, the structural modulation is characterized by breaking of the Ge square lattice into cis−trans chains. This change is more likely the result of weakened Ge−Ge interactions for the middle rare-earth metals (larger size) compared to the late ones (smaller size); in a cooperating fashion, insertion of an Al atom (or transition-metal atom) stabilizes the Ge bonding. This is a highly speculative conjecture, which is evident from the reduced Al concentration in the average structure, concomitant with lanthanide contraction. Following the same trend, one can notice that the Ge2−Ge2 distances became smaller across the family. For instance, the Ge2−Ge2 distance in $LuAl_{0.10(2)}Ge_2$ is 2.7899(4) Å, compared with the distance of 2.872(2) Å in $TbAl_{0.21(2)}Ge_2$. Apparently, the shorter Ge2−Ge2 distance (stronger bonds) mean-stabilized Ge square nets. This, in turn, will suppress the eventual Pierels distortion, which is the case of $TmGe_2$ and $LuGe_2$ with $ZrSi_2$-type structure; these are the only binary phases with this structure.[3c,8a] The remaining members are "missing", and the realization of this bonding arrangement requires doping with Sn or Bi (heavier elements, known to have lesser s−p mixing and a tendency to form hypervalent bonding), as discussed for the RESnGe and $RE[Bi_xGe_{1-x}]_2$ families (RE = Gd−Tm, Lu).[8,39] Generally, the structures of all rare-earth metal digermanides are dependent on the nature (i.e., size) of the rare-earth metal. For example, the early lanthanides (largest atomic size) predominantly form with the $\alpha$-$ThSi_2$ structure type;[1] a gradual transition to an orthorhombically distorted structure (i.e., $\alpha$-$GdSi_2$ structure type; space group *Imma*) is known for the metals in the middle of the lanthanide family.[1] The hexagonal $AlB_2$ structure is prevalent for the late lanthanides (smallest atomic size).[1]

**Electronic Structure Calculations.** Computations of the electronic structures were carried out for $YGe_2$ and the idealized $Y_4AlGe_8$ compound with optimized structures by SIESTA.[28,29] The details of the optimization are given in the SI. Here, we will just point out that the lattice parameters of the optimized $YGe_2$ are $a$ = 4.0902 Å, $b$ = 16.1467 Å, and $c$ = 3.9631 Å, a little smaller than those experimentally observed for $YAl_{0.17(2)}Ge_2$. The lattice parameters of the optimized monoclinic $Y_4AlGe_8$ are $a$ = 5.832 Å, $b$ = 16.1666 Å, $c$ = 11.7791 Å, and $\beta$ = 93.2395°.

The total and partial density of states (DOS) curves are plotted in Figure 7. The Fermi level for $YGe_2$ is located at the bottom of a small valley, but the DOS is not significantly


dx.doi.org/10.1021/ic501002j | *Inorg. Chem.* 2015, 54, 722−732

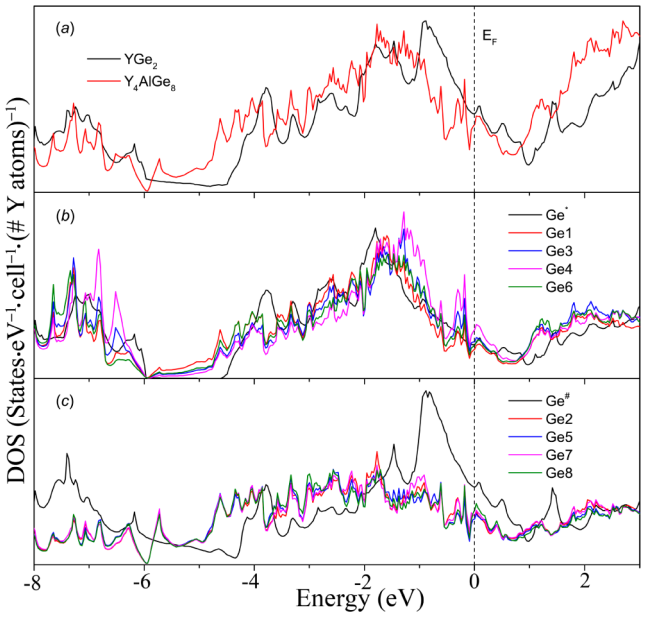


**Figure 7.** Calculated DOS for optimized $YGe_2$ and $Y_4AlGe_8$ (a). The partial DOS is also shown for the zigzag chains (b) and square nets or parallel cis−trans chains (c). Ge* and Ge# represent the Ge atoms within the zigzag chains and square nets in the $YGe_2$ structure. Other Ge atoms are from different sites of the monoclinic structure (see Table S3 in the SI). The energy of the Fermi level is set as a reference at 0 eV.

smaller than the peak DOS just on its right, as shown in Figure 7a. It can also be noted that there is a deeper valley at 0.3 eV and a much deeper valley (or pseudogap) at 1 eV. From this standpoint alone, it seems that the electronic structure could benefit from having more electrons, and experimental evidence suggests that this is indeed the case for $Y(Bi,Ge)_2$.[39] On another hand, the Fermi level of the optimized monoclinic $Y_4AlGe_8$ appears near a peak in the DOS, while there is a deeper valley DOS at −0.09 eV. Using the same argument as that above, we can see that there is a good agreement between this reasoning and the experimentally determined composition $YAl_{0.17(2)}Ge_2$ ($Y_4AlGe_8$═$YAl_{0.25}Ge_2$). However, the DOS valley at −0.09 eV is very narrow, which is indicative of a small stoichiometry breadth and a nearly constant $x$ value in all members of the $REAl_{1-x}Ge_2$ family.

The total DOS for $YGe_2$ shows a large peak just below the Fermi level (up to ca. −1 eV), with several other peaks and a wide pseudogap from −4.5 to −6 eV. In $Y_4AlGe_8$, the DOS is relatively lower from the Fermi level to ca. −1 eV. Many peaks appear below this zone and their extensions to the low-energy zone and almost close the pseudogap, seen in the DOS of $YGe_2$. These characteristics indicate stronger mixing between the orbitals of Y, Al, and Ge in the $Y_4AlGe_8$ structure and the enhanced electronic stability due to breaking of the Ge square nets in $YGe_2$. The point is nicely demonstrated in the partial DOS curves shown in Figure 7b,c. In the zigzag chains, there is only one atomic site for Ge in $YGe_2$. The partial DOS of these Ge atoms, marked as Ge* in Figure 7b, is similar to the total DOS, but notably the large peak near −1 eV is mainly contributed from the other Ge atoms that are engaged in the hypervalent bonding in the square nets. The lower energy of the peaks for Ge* versus Ge# is suggestive of the stability of the zigzag chains relative to the square nets.

Upon accommodation of some Al atoms and suitable structural rearrangement to $Y_4AlGe_8$, the chains distort a little and, because of the lower symmetry (monoclinic) of the structure, are described by four atomic sites. Their partial DOS confirm that all four Ge atoms contribute almost equally, with Ge4 showing the largest deviations in the DOS at the high-energy (−1.5 to −0.5 eV) region, as well as in the lower-energy region (−7 to −6.5 eV). This is likely due to the small distortion in the zigzag pattern, with the Ge4−Ge4 bond being the shortest and therefore strongest. Next in terms of distances is the Ge4−Ge3 bond, and we can see the partial DOS for Ge3 traces the partial DOS for Ge4, albeit the deviations from the average are smaller.

Within the square nets of the $YGe_2$ structure, the long Ge−Ge distance signifies weak bonding. As discussed previously, the square nets break into parallel cis−trans chains, where the distances are closer to normal and the interactions are apparently stronger. In the $Y_4AlGe_8$ structure, these broken slabs are described by four Ge atomic sites. Their partial DOSs are nearly the same, as seen in Figure 7c, but compared with the partial DOS of Ge# in $YGe_2$, the partial DOS of these Ge atoms is much lower, especially just below the Fermi level.

The enhanced stability of the Ge frameworks in the monoclinic structure is more evident in the COHP analysis, as shown in Figure 8. In the $YGe_2$ structure, the Ge−Ge

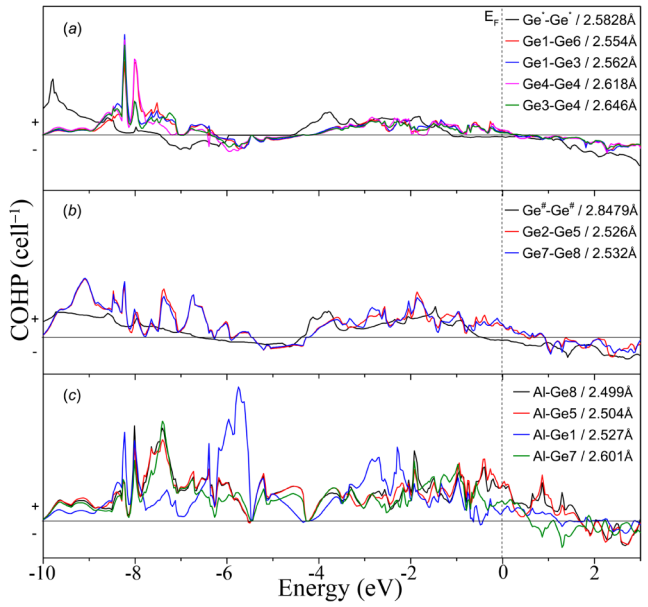


**Figure 8.** Calculated COHP for selected bonds in optimized $YGe_2$ and $Y_4AlGe_8$: (a) bonds within the zigzag chains; (b) bonds within square nets or cis−trans chains; (c) bonds within the Al-centered polyhedron. Ge* and Ge# represent the Ge atoms within the zigzag chains and square nets in the $YGe_2$ structure. Other Ge atoms are from different sites of the monoclinic structure (see Table S3 in the SI).

bonding, within both the zigzag chains and square nets, is in their antibonding states at the Fermi level. Although the total DOS suggests that more electrons would stabilize the structure, such electron enrichment would eventually increase the antibonding character or the Ge−Ge bonds. This is yet another testament to the fact that other factors contribute to the structure stability, with possibly the already discussed Pierels distortion being the most prominent one. In the monoclinic structure, all Ge−Ge bonds show similar COHP and are in


dx.doi.org/10.1021/ic501002j | Inorg. Chem. 2015, 54, 722−732

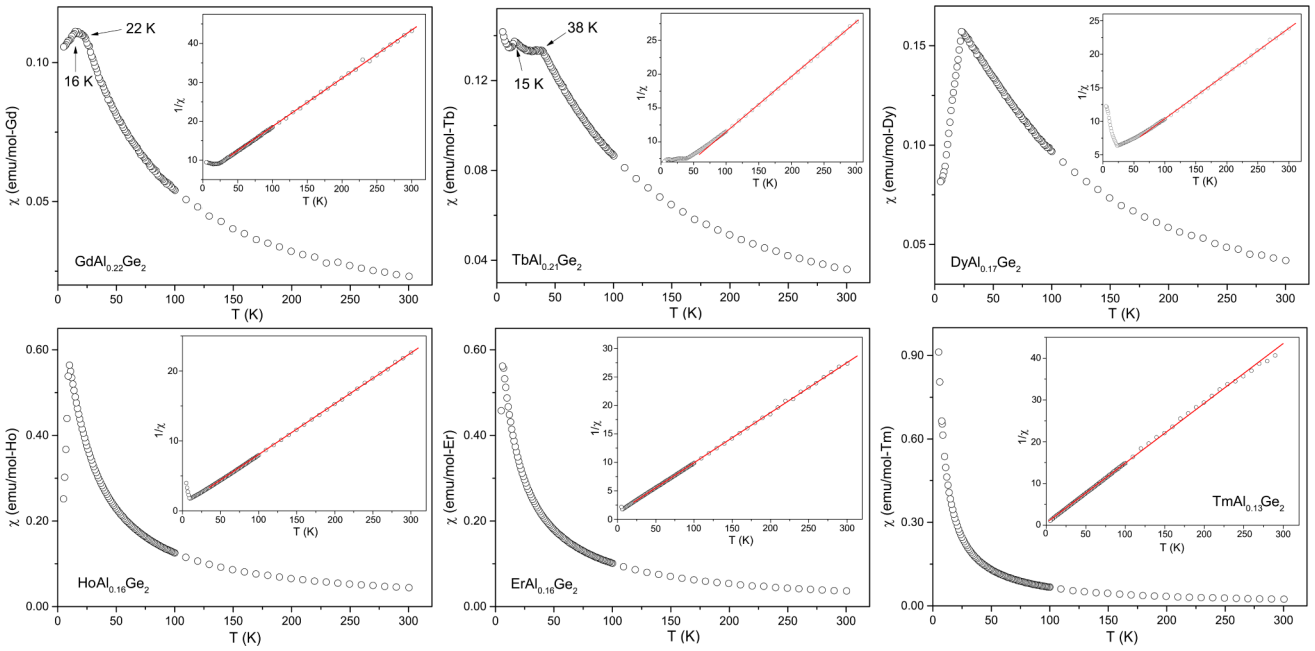


**Figure 9.** Temperature dependence of the magnetic susceptibility $\chi(T)$ for polycrystalline $REAl_{1-x}Ge_2$ samples (RE = Gd−Tm). The insets show the inverse susceptibility $\chi^{-1}(T)$.

their bonding state at the Fermi level (both zigzag and cis−trans chains).

Compared with the Ge−Ge bonds, the Al−Ge bonds show higher COHP values; it should also be noted that all bonds between Al and Ge within cis−trans chains have similar COHP, despite the different distances. The bond between Al and Ge1 within the zigzag chains has a similar distance but shows a much more localized COHP. Clearly, it is the geometry that affects the Al−Ge bond because Ge1 is in a position very different from others in the Al-centered pyramid (Figure S3 in the SI).

**Physical Properties.** The temperature-dependent magnetizations of the $REAl_{1-x}Ge_2$ phases are plotted in Figure 9. The Lu and Y compounds show a flat, Pauli-like $\chi(T)$ dependence and are not presented. From the figure, it is clearly seen that, in the high-temperature regime, all six samples are paramagnetic and obey the Curie−Weiss law $\chi(T) = C/(T - \theta_p)$, where $C = N_A\mu_{eff}^2/3k_B$ is the Curie constant ($k_B$ is the Boltzmann constant, $N_A$ is the Avogadro number, and $\theta_p$ is the paramagnetic Weiss temperature).[40] The Weiss temperatures $\theta_p$ and effective moments $\mu_{eff}$ were obtained from the linear regression of the inverse magnetic susceptibility versus temperature, as shown in the insets in Figure 9, and the numerical values are summarized in Table 4. The observed effective moments are consistent with the values expected for free-ion $RE^{3+}$ species according to Hund's rule.[40]

**Table 4. Selected Magnetic Data for $REAl_{1-x}Ge_2$ (RE = Gd−Tm)**

| compound | $T_N$ (K) | $\theta_p$ (K) | $\mu_{eff}$ ($\mu_B$) | $g[J(J+1)]^{1/2}$ |
|---|---|---|---|---|
| $GdAl_{0.22(2)}Ge_2$ | 22, 16 | −48 | 7.98 | 7.94 |
| $TbAl_{0.21(2)}Ge_2$ | 38, 15 | −44 | 9.90 | 9.72 |
| $DyAl_{0.17(2)}Ge_2$ | 23 | −50 | 10.82 | 10.64 |
| $HoAl_{0.16(2)}Ge_2$ | 10 | −9 | 10.45 | 10.60 |
| $ErAl_{0.15(2)}Ge_2$ | 6 | −13 | 9.57 | 9.58 |
| $TmAl_{0.13(2)}Ge_2$ | <5 | −2 | 7.37 | 7.56 |

The negative $\theta_p$ is suggestive of antiferromagnetic ordering at low temperature, which can also be confirmed by the cusplike features in the $\chi(T)$ plots at low temperatures; the decrease in the magnetic susceptibilities beyond this point is also characteristic of antiferromagnetic ordering. The corresponding Néel temperatures are summarized in Table 4. The dependence of the Néel temperature ($T_N$) on the de Gennes factors $G$ [$G = J(J + 1)(g - 1)^2$, where $J$ is the total angular momentum and $g$ is Landé factor[41]] is plotted in Figure S5 in the SI. The ordering temperatures roughly scale with the de Gennes factors, and two nearly linear regions can be distinguished. This is a good indicator of Ruderman−Kittel−Kasuya−Yosida (RKKY) exchange interactions.[42] Such a coupling mechanism of localized f-electron spins by means of conduction electrons appears to be the norm in rare-earth metal germanides and rare-earth intermetallics in general.[12,43]

In our previous work,[12] empirical relationships between the shortest RE−RE distances and constant s−f exchange coupling energies were developed for select dysprosium and terbium germanides with around the nominal $REGe_2$ composition. On the basis of these relationships and the presented crystallographic data for the average structure of $TbAl_{0.21(2)}Ge_2$, the s−f exchange coupling energy and thus the ordering temperature can be evaluated. Accordingly, in the average structure, the shortest Tb−Tb distance is $R$ = 3.932 Å and the coordination number of the nearest Tb atoms is $Z$ = 4. The constant s−f exchange integral ($J_0$) can be estimated as $J_0/k_B = 67.3-16.56 \times R = 2.818$ K, where $k_B$ is the Boltzmann constant. The exchange energy based on RKKY interactions can be calculated as follows:[42]

$$J_T = -12\pi n J_0 \sum_i F(2k_F R_i) \quad (1)$$

In the above equation, $n$ is the average conduction electron to atom ratio, $F(x)$ is an oscillating function, and $R_i$ is the distance between the central magnetic atom and the $I$th magnetic atom (here only the nearest and second-nearest


dx.doi.org/10.1021/ic501002j | Inorg. Chem. 2015, 54, 722−732

distances were considered). $k_F$ is the Fermi wave factor and can be evaluated based on the free electron model[44]

$$k_F^3 = 3\pi^2 nN/V \quad (2)$$

where $N$ is the total number of atoms in a unit volume $V$. The ordering temperature of the compound can be obtained by the expression[42]

$$k_B T_N = 2/3 J_T G \quad (3)$$

with $G$ being the de Gennes factor (vide supra). The determined ordering temperature using the method is 33 K. Because the Tb−Tb distances in the monoclinic structure vary from that in the average structure, the onset ordering temperature for the modulated structure should be slightly higher than 33 K. In the same way, the ordering temperature of $DyAl_{0.17(2)}Ge_2$ is estimated to be 18 K.

Last, we discuss the possible two-stage transitions that are seen in both Gd and Tb compounds, as emphasized with the arrows in Figure 9. Why two consecutive transitions are see for the Gd and Tb, while the remaining four samples show only one ordering step is not understood at this point. Unrecognized impurity phases are possible but unlikely; the small variation of the Al content and the concomitant changes in the electron concentration are also not believed to be contributing factors. Most likely, the differences in the structural modulations and creation of two magnetic sublattices are the reasons for such behavior.

On this note, we also draw attention to the fact that two-stage ordering is not uncommon in Tb-based compounds and is also seen in other $TbT_{1-x}Ge_2$ (T = transition metal) phases with the same average structure.[13,15] The ordering temperatures of all of these $TbT_{1-x}Ge_2$ (T = Cr,[13a] Mn,[45] Fe,[15] Co,[46] Ni,[47] Cu[47]) compounds, as well as $TbAl_{0.21(2)}Ge_2$, are shown in Figure 10. The Tb metal even shows more than one ordering

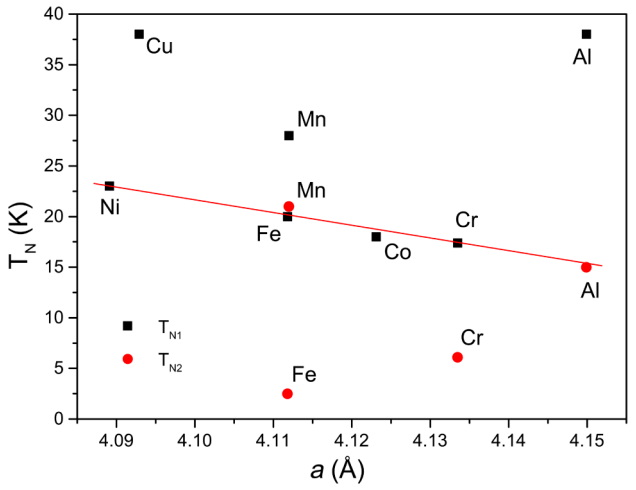


**Figure 10.** Néel temperatures of some $TbM_{1-x}Ge_2$ compounds, reported as isotypic with $CeNi_{1-x}Si_2$. The $T_N$'s are plotted versus the corresponding lattice constant $a$.

transition itself because of its complex f-band characteristics.[48] Magnetization data reported for $Tb_4FeGe_8$ single crystals indicate two transitions corresponding to ordering in the basal plane and along the long axis.[15] It is evident that the compounds with Al and Cu have higher ordering temperatures than the others, particularly those containing transition metals with partially filled d bands.[47] These observations are intriguing and lead to the question, is it possible that ferrimagnetic correlations also exist between the Tb and transition-metal atoms, thereby depressing the ordering temperatures?

To try to answer this question, we recall that, in the case of ferrimagnetic ordering, the inverse susceptibility versus temperature is not linear but rather hyperbolic above the ordering temperature. However, all of these $TbT_{1-x}Ge_2$ compounds show perfect linearity in these regions. The effective moments are also close to the theoretical value of free ion $Tb^{3+}$, which is suggestive of no magnetic contribution from the transition metals; this conjecture has been confirmed by neutron diffraction experiments, at least for some of the compounds in question.[49] In this view, the RKKY exchange interaction should dominate their magnetic behaviors, in good agreement with the results discussed in the paragraphs above. Generally, the RKKY exchange interaction has an oscillating character, as described by eq 1. In the $TbT_{1-x}Ge_2$ family, both $k_F$ and the unit cell should change slightly because $x$ is typically greater than $^1/_2$ (i.e., occupation factors are below 50%) and the variations among the transition-metal occupancies are not significant. For such small changes, the oscillating function can be approximated linearly. A linear relationship between the lattice constant $a$ and ordering temperatures is obvious, as shown by the red line in Figure 10. Neutron diffraction show that magnetic ordering in $TbCr_{0.30}Ge_2$ is described by a propagation vector $k$ = ($^1/_2$, 0, 0); the second magnetic ordering in $TbMn_{0.33}Ge_2$ corresponds to a change of the propagation vector from $k$ = (0, 0.1134, 0) to $k$ = (0.1097, 0, 0).[45] It should be noted that, in $TbMn_{0.33}Ge_2$, the propagation vector does not change its length significantly but its angle; thus, it is difficult to detect the second transition in the magnetic measurements. A clear linear relationship describes the ordering in the basal plane in the structure, as reported in $TbFe_{0.25}Ge_2$.[15] The compounds with Ni, Cu, and Co may be this case or have a second transition below the limit of measurements. We can therefore reason that the two magnetic transitions in $TbAl_{0.21(2)}Ge_2$ could correspond to the ordering of the Tb moments along the crystallographic $b$ axis and in the $ac$ plane, respectively, and that further work by neutron diffraction, preferably single-crystal XRD, will be needed to fully understand the magnetism in this series.

## CONCLUSIONS

Rare-earth metal aluminum germanides with the general formula $REAl_{1-x}Ge_2$ (RE = Gd, Tb, Dy, Ho, Er, Tm, Lu, and Y) have been synthesized and structurally characterized by XRD and electron diffraction. These compounds have an average structure with the orthohombic $CeNi_{1-x}Si_2$ type but exhibit clear incommensurate modulations, close to 4-fold the commensurate superstructure described in an earlier publication for $Tb_4FeGe_8$.[15] Electronic structure calculations confirm the instability of the Ge square nets in the average structure and lend support to the idea that structural distortion to cis−trans chains will be favored. The magnetic response of polycrystalline $REAl_{1-x}Ge_2$ samples shows dominating RKKY interactions; ideas correlating the ordering temperatures within the $TbT_{1-x}Ge_2$ (T = transition metal) family have been put forward.

## ASSOCIATED CONTENT

### Supporting Information

Tables with atomic coordinates and equivalent displacement parameters of $YAl_{0.17(2)}Ge_2$, principal mean-square atomic


dx.doi.org/10.1021/ic501002j | Inorg. Chem. 2015, 54, 722−732

displacements in $YAl_{0.17(2)}Ge_2$, atomic coordinates of the optimized $Y_4AlGe_8$ and $YGe_2$, and selected atomic distances in $YGe_2Al_{0.17}$ and the optimized $Y_4AlGe_8$ and $YGe_2$, figures showing experimental and simulated powder XRD patterns, thermal analysis, and selected SAED patterns of $TbAl_{0.21(2)}Ge_2$ and representing the crystal structures of the optimized $Y_4AlGe_8$, and plots of the Néel temperature of $REAl_{1-x}Ge_2$ against the corresponding $RE^{3+}$ de Gennes factors. This material is available free of charge via the Internet at http://pubs.acs.org.

## AUTHOR INFORMATION


### Corresponding Author

*E-mail: bobev@udel.edu. Fax: (302) 831-6335.


### Author Contributions

The manuscript was written through contributions of all authors. All authors have given approval to the final version of the manuscript.

### Notes

The authors declare no competing financial interest.

## ACKNOWLEDGMENTS

S.B. acknowledges financial support from the National Science Foundation through Grant DMR-0743916 (CAREER).

## REFERENCES


(1) Villars, P., Calvert, L. D., Eds. *Pearson's Handbook of Crystallographic Data for Intermetallic Phases*, 2nd ed.; ASM International: Materials Park, OH, 1991, and the desktop edition, 1997.

(2) *Inorganic Crystal Structure Database (ICSD)*, version 2.2.2; Fachinformationszentrum Karlsruhe: Karlsruhe, Germany, Nov 2013.

(3) (a) Bobev, S.; Bauer, E. D.; Thompson, J. D.; Sarrao, J. L.; Miller, G. J.; Eck, B.; Dronskowski, R. *J. Solid State Chem.* **2004**, *177*, 3545. (b) Schobinger Papamantellos, P.; de Mooij, D. B.; Bushchow, K. H. J. *J. Less-Common Met.* **1988**, *144*, 265. (c) Francqis, M.; Venturini, G.; Malaman, B.; Roques, B. *J. Less-Common Met.* **1990**, *160*, 197.

(4) (a) Salamakha, P. S.; Sologub, O. L.; Demcheko, P.; Righi, L.; Bocelli, G. *J. Alloys Compd.* **2001**, *315*, L1. (b) Sekizawa, K. J. *Phys. Soc. Jpn.* **1966**, *21*, 1137. (c) Boutarek, N.; Pierre, J.; Lambertandron, B.; Leritier, P.; Madar, R. *J. Alloys Compd.* **1994**, *204*, 251. (d) Mulder, F. M.; Thiel, R. C.; Buschow, K. H. J. *J. Alloys Compd.* **1994**, *205*, 169. (e) Zaharko, O.; Schobinger Papamantellos, P.; Ritter, C.; Janssen, Y.; Brueck, E.; de Boer, F. R.; Buschow, K. H. J. *J. Phys.: Condens. Matter* **1998**, *10*, 2881. (f) Zan, J. A.; Yuen, T.; Lin, C. L.; Huang, X. Y.; Li, J. *J. Appl. Phys.* **2003**, *93*, 8340.

(5) Massalski, T. B., Ed. *Binary Alloys Phase Diagrams*; ASM International: Materials Park, OH, 1990.

(6) (a) Guloy, A. M.; Corbett, J. D. *Inorg. Chem.* **1991**, *30*, 4789. (b) Budnyk, S.; Weitzer, F.; Kubata, C.; Prots', Yu.; Aksel'rud, L. G.; Schnelle, W.; Hiebl, K.; Nesper, R.; Wagner, F. R.; Grin', Yu. *J. Solid State Chem.* **2006**, *179*, 2329. (c) Morozkin, A. V.; Seropegin, Yu. D. *J. Alloys Compd.* **2004**, *365*, 168.

(7) (a) Tobash, P. H.; Lins, D.; Bobev, S.; Hur, N.; Thompson, J. D.; Sarrao, J. L. *Inorg. Chem.* **2005**, *45*, 7286. (b) Zhang, J.; Tobash, P. H.; Pryz, W.; Buttery, D.; Hur, N.; Thompson, J. D.; Sarrao, J. L.; Bobev, S. *Inorg. Chem.* **2013**, *52*, 953. (c) Christensen, J.; Lidin, S.; Malaman, B.; Venturini, G. *Acta Crystalogr., Sect. B* **2008**, *64*, 272. (d) Shcherban, O.; Savysyuk, I.; Semuso, N.; Gladyshevskii, R.; Cenzual, K. *Chem. Met. Alloys* **2009**, *2*, 115. (e) Venturini, G.; Ijjaali, I.; Malaman, B. *J. Alloys Compd.* **1999**, *284*, 262. (f) Tobash, P. H.; Bobev, S.; Thompson, J. D.; Sarrao, J. L. *J. Alloys Compd.* **2009**, *488*, 533.

(8) (a) Tobash, P. H.; Meyers, J. J.; DiFilippo, G.; Bobev, S.; Ronning, F.; Thompson, J. D.; Sarrao, J. L. *Chem. Mater.* **2008**, *20*, 2151. (b) Tobash, P. H.; Bobev, S.; Ronning, F.; Thompson, J. D.; Sarrao, J. L. *J. Alloys Compd.* **2009**, *488*, 511.

(9) (a) Tobash, P. H.; Lins, D.; Bobev, S. *Chem. Mater.* **2005**, *17*, 5567. (b) Suen, N. Z.; Tobash, P. H.; Bobev, S. *J. Solid State Chem.* **2011**, *184*, 2941. (c) Guo, S. P.; Meyers, J. J.; Tobash, P. T.; Bobev, S. *J. Solid State Chem.* **2012**, *192*, 16.

(10) Bobev, S.; Tobash, P. H.; Fritsch, V.; Thompson, J. D.; Hundley, M. F.; Sarrao, J. L.; Fisk, Z. *J. Solid State Chem.* **2005**, *178*, 2091.

(11) Darone, G. M.; Hmiel, B.; Zhang, J.; Saha, S.; Kirshenbaum, K.; Greene, R.; Paglione, J.; Bobev, S. *J. Solid State Chem.* **2013**, *201*, 191.

(12) Zhang, J.; Bobev, S. *Inorg. Chem.* **2013**, *52*, 5307.

(13) (a) Bie, H. Y.; Tkachuk, A. V.; Mar, A. *J. Solid State Chem.* **2009**, *182*, 122. (b) Gil, A.; Kaczorowski, D.; Penc, B.; Hoser, A.; Szytula, A. *J. Solid State Chem.* **2011**, *184*, 227. (c) Gil, A.; Leciejewicz, J.; Maletka, K.; Szytula, A.; Tomkowicz, Z.; Wojciechowski, K. *J. Magn. Magn. Mater.* **1994**, *129*, L155. (d) Venturini, G.; Francqis, M.; Malaman, B.; Roques, B. *J. Less-Common Met.* **1990**, *160*, 215.

(14) Salamakha, P. S. In *Handbook on the Physics and Chemistry of Rare Earths*; Gschneidner, K. A., Jr, Eyring, L., Eds.; Elsevier: Amsterdam, The Netherlands, 1999; Vol. 27.

(15) Zhuravleva, M. A.; Bilc, D.; Pcionek, R. J.; Mahanti, S. D.; Kanatzidis, M. G. *Inorg. Chem.* **2005**, *44*, 2177.

(16) *SMART*; Bruker Analytical X-ray Systems, Inc.: Madison, WI, 2003.

(17) *SAINT NT*, version 6.45; Bruker Analytical X-ray Systems, Inc.: Madison, WI, 2003.

(18) Sheldrick, G. M. *SADABS*; University of Göttingen: Göttingen, Germany, 2003.

(19) Sheldrick, G. M. *SHELXTL*; University of Göttingen: Göttingen, Germany, 2001.

(20) Venturini, G.; Ljjaali, I.; Malaman, B. *J. Alloys Compd.* **1999**, *288*, 183 . Elemental analysis had not been performed, and this phase may very well be impurity-stabilized..

(21) The CIF have also been deposited with Fachinformationszentrum Karlsruhe [76344 Eggenstein, Leopoldshafen, Germany; fax (49) 7247-808-666; email crysdata@fiz.karlsruhe.de; depository numbers CSD-427641 ($GdAl_{0.22(2)}Ge_2$), CSD-427642 ($TbAl_{0.21(2)}Ge_2$), CSD-427643 ($DyAl_{0.17(2)}Ge_2$), CSD-427644 ($HoAl_{0.16(2)}Ge_2$), CSD-427645 ($ErAl_{0.15(2)}Ge_2$), CSD-427646 ($TmAl_{0.13(2)}Ge_2$), CSD-427647 ($LuAl_{0.10(2)}Ge_2$), and CSD-427648 ($YAl_{0.17(2)}Ge_2$)].

(22) Tank, R.; Jepsen, O.; Burkhardt, A.; Andersen, O. K. *The TB-LMTO-ASA program*, version 4.7; Max-Plank-Institut fur Festkörperforschung: Stuttgart, Germany, 1994.

(23) Jepsen, O.; Andersen, O. K. *Z. Phys. B* **1995**, *97*, 35.

(24) Blöchl, P. E.; Jepsen, O.; Andersen, O. K. *Phys. Rev. B* **1994**, *49*, 16223.

(25) Anderson, O. K.; Jepsen, O. *Phys. Rev. Lett.* **1984**, *53*, 2571.

(26) Lambrecht, W. R. L.; Andersen, O. K. *Phys. Rev. B* **1986**, *34*, 2439.

(27) Dronskowski, R.; Blöchl, P. E. *J. Phys. Chem.* **1993**, *97*, 8617.

(28) Ordejón, P.; Artacho, E.; Soler, J. M. *Phys. Rev. B* **1996**, *53*, R10441.

(29) Soler, J. M.; Artacho, E.; Gale, J. D.; García, A.; Junquera, J.; Ordejón, P.; Sánchez-Portal, D. *J. Phys.: Condens. Matter* **2002**, *14*, 2745.

(30) Troullier, N.; Martins, J. L. *Phys. Rev. B* **1991**, *43*, 1993.

(31) Perdew, J. P.; Burke, K.; Emzerhof, M. *Phys. Rev. Lett.* **1996**, *77*, 3865.

(32) (a) Zeng, L. M.; He, J. J.; Qin, P. L.; Wei, X. Z. *Powder Diff.* **2008**, *23*, 60. (b) Zeng, L. M.; Qin, P. L.; Chen, Y. Q.; Liu, H. R.; He, W.; Nong, L. Q. *Mater. Chem. Phys.* **2008**, *112*, 934. (c) Qin, P. L.; Chen, Y. Q.; Liu, H. Y.; Nong, L. Q.; Zeng, L. M. *J. Alloys Compd.* **2008**, *463*, 34.

(33) Pukas, S. Ya.; Kuprisyuk, V. V.; Mel'nik, A. L.; Semus'o, N. Z.; Gladyshevskii, R. E. *Ukr. Khim. Zh.* **2006**, *72*, 16.

(34) Buschow, K. H. J.; Schobinger Papamantellos, P.; Fischer, P. *J. Less-Common Met.* **1988**, *139*, 221.

(35) Pauling, L. *The Nature of the Chemical Bond*; Cornell University Press: Ithaca, NY, 1960.

(36) (a) Haussermann, U.; Amerioun, S.; Eriksson, L.; Lee, C. S.; Miller, G. J. *J. Am. Chem. Soc.* **2002**, *123*, 4371. (b) Li, B.; Corbett, J.

D. *Inorg. Chem.* **2007**, *46*, 8812. (c) Seo, D. K.; Corbett, J. D. *J. Am. Chem. Soc.* **2000**, *122*, 9621. (d) Zhang, J.; Bobev, S. *J. Solid State Chem.* **2013**, *205*, 21.
(37) (a) Tremel, W.; Hoffmann, R. *J. Am. Chem. Soc.* **1987**, *109*, 124. (b) Tremel, W.; Hoffmann, R. *Inorg. Chem.* **1987**, *26*, 118. (c) Keszler, D.; Hoffmann, R. *J. Am. Chem. Soc.* **1987**, *109*, 118.
(38) Makongo, J. P. A.; Suen, N. T.; Guo, S. P.; Saha, S.; Greene, R.; Paglione, J.; Bobev, S. *J. Solid State Chem.* **2014**, *211*, 95.
(39) Zhang, J.; Hmiel, B.; Antonelli, A.; Tobash, P. H.; Bobev, S.; Saha, S.; Kirshenbaum, K.; Greene, R. L.; Paglione, J. *J. Solid State Chem.* **2012**, *196*, 586.
(40) Smart, J. S. *Effective Theories of Magnetism*; Saunders: Philadelphia, PA, 1996.
(41) de Gennes, P. G. *J. Phys. Radium* **1962**, *23*, 510.
(42) (a) Yosida, K.; Miwa, M. J. *J. Appl. Phys.* **1961**, *32*, 85. (b) Kaplan, T. A. *Phys. Rev.* **1961**, *124*, 329. (c) Elliott, R. J. *Phys. Rev.* **1961**, *124*, 246.
(43) Wohlfarth, E. P., Ed. *Handbook of Magnetic Materials*; North-Holland Publishing Company: Amsterdam, The Netherlands, 1980; Chapter 4.
(44) Kittel, K. *Introduction of Solid State Physics*, 8th ed.; Wiley: New York, 2005.
(45) (a) Gil, A.; Leciejewicz, J.; Maletka, K.; Szytuła, A.; Tomkowicz, Z.; Wojciechowski, K. *J. Magn. Magn. Mater.* **1994**, *129*, L155. (b) Gil, A.; Hoffmann, M.; Penc, B.; Szytuła, A. *J. Alloys Compd.* **2001**, *320*, 29.
(46) Baran, S.; Henkel, F.; Kaczorowski, D.; Hernández-Velasco, J.; Penc, B.; Stüßer, N.; Szytuła, A.; Wawrzyńska, E. *J. Alloys Compd.* **2006**, *415*, 1.
(47) Schobinger-Papamantellos, P.; Bushchow, K. H. J. *J. Alloys Compd.* **1992**, *187*, 73.
(48) Lang, J. K.; Baer, Y.; Cox, P. A. *J. Phys. F: Met. Phys.* **1981**, *11*, 121.
(49) Gil, A.; Kaczorowski, D.; Penc, B.; Hoser, A.; Szytuła, A. *J. Solid State Chem.* **2011**, *184*, 227.